electronics

MDPI

Article

High-Precision Main Shaft Displacement Measurement for Wind Turbines Using an Optimized Position-Sensitive Detector

Weitong Zhang [1], Lingyun Wang [1,*], Guangxi Li [2], Huicheng Zheng [1] and Chengwei Pang [1]

[1] School of Optoelectronic Engineering, Changchun University of Science and Technology, Changchun 130022, China; 2022100364@mails.cust.edu.cn (W.Z.); 2022100361@mails.cust.edu.cn (H.Z.); 2022100396@mails.cust.edu.cn (C.P.)

[2] College of Electronic Information Engineering, Changchun University, Changchun 130022, China; ligq@ccu.edu.cn

* Correspondence: 1999800022@cust.edu.cn

Abstract: The main shaft of a wind turbine is a critical component that ensures the normal operation of the turbine, and its axial displacement directly impacts its efficiency and safety. The inaccurate measurement of axial displacement may lead to severe issues such as shaft fractures, causing turbine shutdowns. Correcting measurement errors related to axial displacement is essential to prevent potential accidents. This study proposes an improved error correction method for measuring the axial displacement of wind turbine main shafts. Using a position-sensitive detector (PSD) and laser triangulation, the axial and radial displacements of the main shaft are measured to address environmental interference and cost constraints. Additionally, a Sparrow Search Algorithm- Backpropagation (SSA-BP) model is constructed based on operational data from the wind turbine's main shaft to correct the system's nonlinear errors. The Sparrow Search Algorithm (SSA) is employed to optimize the weights and thresholds of the Backpropagation (BP) neural network, enhancing prediction accuracy and model stability. Initially, a main shaft displacement measurement system based on a precision displacement stage was developed, and system stability tests and displacement measurement experiments were conducted. The experimental results demonstrate that the system stability error is ±0.025 mm, which is lower than the typical error of 0.05 mm in contact measurement. After model correction, the maximum nonlinear errors of the axial and radial displacement measurements are 0.83% and 1.29%, respectively, both of which are lower than the typical measurement error of 2% in contact measurements. This indicates that the proposed model can reliably and effectively correct the measurement errors. However, further research is still necessary to address potential limitations, such as its applicability in extreme environments and the complexity of implementation.

Keywords: PSD; main shaft displacement; laser triangulation; SSA-BP neural network

Citation: Zhang, W.; Wang, L.; Li, G.; Zheng, H.; Pang, C. High-Precision Main Shaft Displacement Measurement for Wind Turbines Using an Optimized Position-Sensitive Detector. *Electronics* **2024**, *13*, 5055. https://doi.org/10.3390/electronics13245055

Academic Editors: Yeongsu Bak and Sesun You

Received: 28 November 2024
Revised: 16 December 2024
Accepted: 19 December 2024
Published: 23 December 2024

1. Introduction

The main shaft, as a key component connecting the blades and the generator, is an essential transmission element in wind turbine systems. In China, most wind turbines are located in regions prone to low temperatures, strong winds, sandstorms, or high humidity and coastal areas with severe corrosion, where the main shaft is particularly susceptible to fractures, potentially leading to accidents [1–4].

In January 2011, a wind turbine in the Dali Dafengba Wind Farm operated by Huaneng witnessed a main shaft fracture accident on turbine No. 60. The reason for this was that excessive main shaft displacement caused by improper machining led to fatigue failure [4]. Reports indicate that certain models of wind turbines have encountered premature main shaft fractures after just four years of operation [5]. These failures have resulted in significant economic losses for wind farms. According to information from wind power stations, dozens of wind turbines have suffered main shaft fractures during the early stages

of use. Such premature failures not only directly damage the equipment but also lead to unexpected shutdowns, further disrupting power generation schedules. This, in turn, incurs additional costs for emergency repairs and results in revenue losses [6,7]. Studies suggest that main shaft failures in wind turbines may contribute to millions of dollars in losses annually, with some individual wind farms reporting losses in the range of tens to hundreds of thousands of dollars per incident [8]. Operation and maintenance (O&M) costs for wind turbines can account for 10–20% of the total cost of a wind energy project, and this percentage can rise to 35% by the end of a turbine's service life [9].

The main shaft displacement is a critical indicator used to assess the health of the main shaft. It directly affects the stability of turbine operation and the reliability of the transmission system. Variations in the shaft displacement reflect the relative motion between the main shaft and other key components, such as bearings and the gearbox. To ensure the safe and stable operation of the wind turbine, precise monitoring of the main shaft displacement is necessary [10,11]. Excessive displacement can lead to poor alignment between the main shaft and other critical components, such as bearings and the gearbox, increasing friction and wear. This accelerates bearing damage and may even cause bearing failure, impacting the entire turbine's normal operation. Furthermore, excessive displacement can cause vibrations and noise, raising the risk of mechanical failure, reducing the efficiency of the turbine's transmission system, and decreasing power generation efficiency. In extreme cases, it may even lead to catastrophic failures, such as the main shaft.

In recent years, domestic and international researchers have continuously explored monitoring the state of wind turbine main shafts. Traditional monitoring methods largely rely on contact sensors, with vibration monitoring being the predominant technique [12].

Zimroz R et al. [13] installed accelerometer vibration sensors on a wind turbine to monitor the vibration of the main shaft and detect potential faults. Cheng J et al. [14] developed an online monitoring system using ultrasonic excitation and reception devices to achieve the real-time monitoring of main shaft quality. However, these systems are often affected by noise, which compromises their reliability and accuracy. Jiang Z et al. [15] used infrared sensors for the fault detection of turbine main shafts, but the high cost of infrared equipment limits its widespread application. Selvaraj Y et al. [16] proposed a wind turbine main shaft monitoring method combining IoT and machine learning technologies, which improves fault prediction capabilities through real-time data collection and intelligent analysis. However, its high computational requirements for large-scale data processing limit its applicability in resource-constrained environments. To address the issues of noise interference and high equipment costs in the aforementioned methods, this paper designs a non-contact, high-precision detection method for main shaft axial displacement. This method not only maintains high monitoring accuracy in complex environments but also significantly reduces the overall system operational cost.

During the operation of wind turbines, environmental noise caused by high-speed rotation, airflow disturbances, and mechanical vibrations significantly interfere with measurements made by traditional contact sensors. To address this issue, this study adopts an optical non-contact sensor and utilizes a PSD as the core component. PSD position sensors are a type of photoelectric distance measurement device that determines the position by detecting the photocurrent corresponding to the energy center of the light spot on the sensor's photosensitive area. Compared to other non-contact technologies, PSDs offer significant advantages: first, PSD measurements are solely related to the geometric center of the light spot and are not strictly dependent on its shape, enabling stable measurements even when the light spot shape changes. Second, PSDs have fast response speeds, allowing real-time detection and feedback of positional information. Furthermore, PSDs have a high resolution, enabling precise position measurements and ensuring measurement accuracy in complex environments [17,18]. Similarly, compared to capacitive sensors, which are sensitive to environmental humidity and material properties, PSD technology is more

stable and less affected by environmental factors. This makes PSDs particularly suitable for dynamically changing environments, enabling continuous and accurate measurements [19].

Laser Triangulation is a non-contact displacement measurement method based on optical principles, commonly used for high-precision distance or displacement measurements. The basic principle involves projecting a laser beam onto the surface of an object, with the reflected light being received by a detector. The displacement of the object is measured by analyzing the angular changes in the reflected light [20,21]. When combined with a PSD, the performance of laser triangulation is significantly enhanced. PSDs feature high sensitivity and fast response, enabling more precise detection of changes in the position of the reflected light, thereby improving the accuracy of displacement measurements. Moreover, the real-time feedback capability of PSDs further optimizes the measurement process, allowing the system to adapt better to complex measurement environments, enhance its resistance to interference, and achieve more efficient signal processing [22].

However, despite the numerous advantages of PSD sensors, certain nonlinear errors persist in practical applications, particularly when the light spot approaches the edge of the sensor, where the output signal may deviate from linearity. To overcome these errors and improve measurement accuracy, this paper proposes the use of a Sparrow Search Algorithm (SSA) to optimize a BP neural network. Since BP neural networks are often prone to being trapped in local optima, which limits significant improvements in prediction accuracy, the SSA is used to optimize the weights and thresholds of the BP network. By introducing an advanced error correction algorithm, the aim is to effectively reduce the impact of environmental interference and equipment nonlinearity on measurement results. This will enable the precise monitoring of the main shaft displacement, providing reliable technical support for the health management and safe operation of wind turbine systems.

2. The Measurement Principle of Wind Turbine Main Shaft Displacement

The internal structure of a wind turbine, as shown in Figure 1, mainly includes the blades, hub, pitch system, main shaft, gearbox, generator, nacelle and other components [23]. The main shaft, as a critical load-bearing part, is responsible for transferring the kinetic energy generated by the blades to the gearbox.

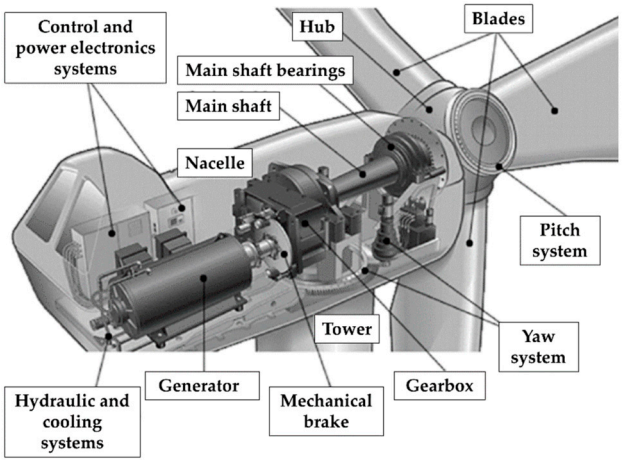

Figure 1. Internal structure of a wind turbine.

As shown in Figure 2, during operation, the horizontal force F_{xn} on the main shaft mainly results from the overturning force and centrifugal force from the blades, as well as the braking force applied to the main shaft during the activation of the mechanical brake system. The radial force F_{zn} on the main shaft primarily comes from the gravitational forces acting on the main shaft, gearbox, and other components. Therefore, during the operation of the wind turbine main shaft, in addition to axial displacement, radial displacement also occurs [24]. These two types of displacement can impact the stability of the main shaft and the overall performance of the wind turbine.

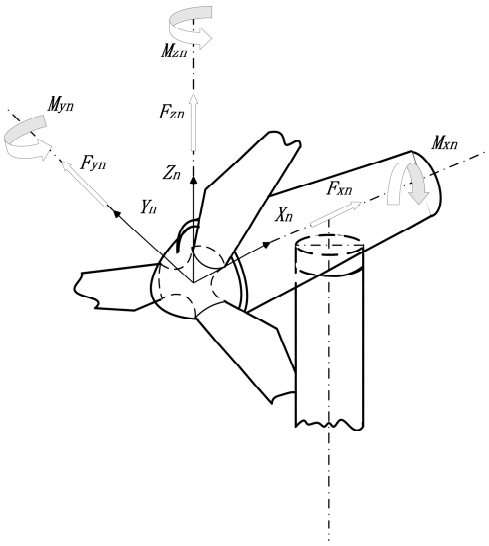

Figure 2. Analysis of the forces acting on the main shaft of the wind turbine.

Axial displacement of the main shaft is directly transferred to the input shaft of the gearbox, causing both the planetary gears and the carrier to move axially. This can lead to wear on the gear surfaces of the planetary gears and potentially damage other components within the gearbox, ultimately causing gearbox failure and turbine shutdown. Therefore, axial displacement has a detrimental effect on the bearings supporting the planetary gear carrier in the gearbox.

Radial displacement of the main shaft can result in bearing damage, gearbox failures, and uneven wear of other mechanical components, reducing their service life. The mechanical imbalance caused by displacement increases generator vibration and noise. Prolonged radial displacement may lead to mechanical failures or even significant damage to the generator, impacting the reliability of the entire wind turbine [25].

To prevent axial and radial displacement from interfering with the operation of wind turbine systems, this paper uses the laser triangulation method to measure the axial and radial displacement of the wind turbine main shaft.

2.1. Working Principle

Laser triangulation includes both direct laser triangulation and oblique laser triangulation. Compared to direct laser triangulation, oblique laser triangulation offers a larger measurement range and higher stability. In this method, the laser beam is directed at a specific angle to the object, allowing the reflected light to be more evenly distributed, which reduces the impact of variations in reflection direction on measurement accuracy. Additionally, the oblique method effectively avoids issues such as the overlap of the incident and sensor-received light, making it more suitable for complex measurement environments. It is particularly effective for measuring objects with smooth or irregular surfaces. This system adopts the oblique laser triangulation method for measurements.

The basic principle for measuring the axial and radial displacement of the main shaft involves fixing a reflector to the surface of the main shaft. A laser beam is projected through a converging lens directly onto the surface of the reflector. The reflected laser beam is then projected onto the photosensitive surface of a PSD. By reading the geometric centroid of the light spot and using a signal processing unit to convert this into a voltage signal, the data are transmitted to an A/D acquisition chip for further processing. The measurement principle is illustrated in Figure 3.

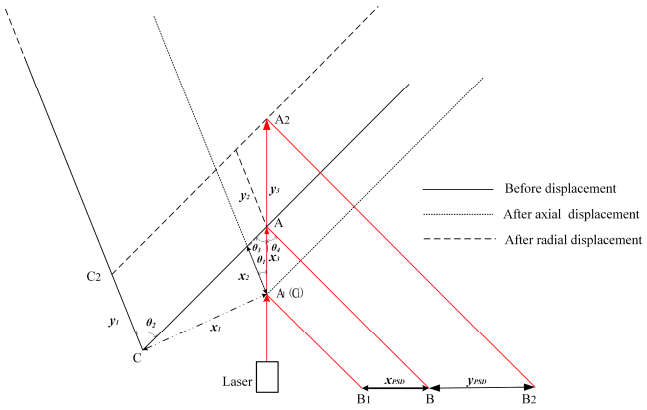

Figure 3. Schematic of main shaft displacement measurement principle.

The solid line represents the position of the wind turbine main shaft before displacement. The laser strikes point A on the main shaft surface, is reflected by the mirror, and lands at point B on the PSD photosensitive surface.

The dashed line 1 represents the position after axial displacement, where the laser hits point A_1 on the main shaft surface, is reflected by the mirror, and lands at point B_1 on the PSD surface. The displacement between points C and C_1, denoted as x_1, represents the axial displacement of the main shaft, while the displacement between points B and B_1, denoted as x_{PSD}, represents the displacement of the light spot on the PSD surface.

The dashed line 2 represents the position after radial displacement, where the laser strikes point D on the main shaft surface, is reflected by the mirror, and lands at point B_2 on the PSD surface. The displacement between points C and C_2, denoted as y_1, represents the radial displacement of the main shaft, while the displacement between points B and B_2, denoted as y_{PSD}, represents the displacement of the light spot on the PSD surface.

The angles θ_1, θ_2, θ_3 and θ_4 are defined as follows: θ_1 is the angle between the main shaft and the ground, θ_2 is the angle between the reflector and the radial direction of the main shaft, θ_3 is the angle between the laser's incident direction and the reflector, and θ_4 is the angle between the laser's incident direction and the surface normal of the main shaft.

From geometric relationships, it can be determined that $\theta_3 = \theta_2 - \theta_1$ and $\theta_4 = \pi - 2\theta_3$. Based on the trigonometric relationship in Equation (1), the linear relationship between the axial displacement x_1 and the horizontal displacement of the light spot on the PSD photosensitive surface x_{PSD} can be derived, as shown in Equation (2).

$$\begin{cases} x_2 = \frac{x_1}{\tan\theta_2} \\ x_3 = x_2 \frac{\sin\theta_2}{\sin(\theta_2 - \theta_1)} \\ x_{PSD} = x_3 \tan(2\theta_2 - 2\theta_1) \end{cases} \tag{1}$$

which can be simplified to

$$x_1 = -x_{PSD} \frac{\sin(\theta_2 - \theta_1)}{\cos\theta_2 \tan(2\theta_2 - 2\theta_1)} \tag{2}$$

Similarly, based on the trigonometric relationship in Equation (3), the linear relationship between the radial displacement y_1, and the horizontal displacement of the light spot on the PSD photosensitive surface, y_{PSD} can be derived, as shown in Equation (4).

$$\begin{cases} y_2 = y_1 \\ y_3 = y_2 \frac{\sin\theta_2}{\sin(\theta_2 - \theta_1)} \\ y_{PSD} = y_3 \tan(2\theta_2 - 2\theta_1) \end{cases} \tag{3}$$

which can be simplified to:

$$y_1 = -y_{PSD} \frac{\sin(\theta_2 - \theta_1)}{\sin\theta_2 \tan(2\theta_2 - 2\theta_1)} \tag{4}$$

In these equations, x_1 represents the axial displacement of the main shaft, y_1 represents the radial displacement of the main shaft, θ_1 is the angle between the main shaft and the ground, θ_2 is the angle between the reflector and the radial direction of the main shaft, x_{PSD} is the horizontal displacement of the light spot on the PSD for axial displacement, and y_{PSD} is the horizontal displacement of the light spot on the PSD for radial displacement.

After simplification, it can be concluded that the axial and radial displacement of the wind turbine main shaft is linearly related to the displacement of the light spot on the PSD photosensitive surface, and this relationship only depends on the angle between the main shaft and the ground θ_1 and the angle between the reflector and the radial direction of the main shaft θ_2.

2.2. Overall System Structure

The wind turbine main shaft displacement measurement system consists of a 2D PSD, PSD signal processing circuit, main controller (STM32F429), and high-speed A/D conversion chip (AD7606). The overall structure is shown in Figure 4 The 2D PSD receives the light spot reflected from the mirror and converts it into a current signal. This signal is processed by the PSD signal processing circuit and converted into a voltage signal suitable for processing by the AD7606. The main controller, STM32F429, is responsible for displacement calculations and determining the main shaft's displacement after processing the data. The system uses USB communication combined with RL-USB and USB-Host protocols, allowing the STM32's Micro-USB interface to connect to a Micro-SD card for storing main shaft displacement data. The system utilizes RL-TCPnet to upload the collected displacement data to a remote computer. The remote computer, using the FlashFxp 5.1.0 client, retrieves and manages the displacement data from the Micro-SD card over long distances.

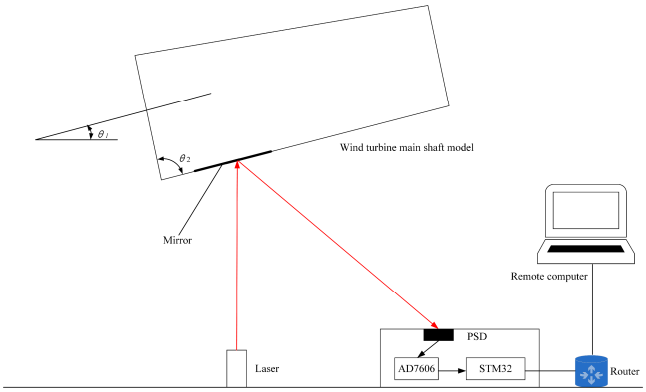

Figure 4. Structure of the wind turbine main shaft displacement measurement system.

3. Factors Affecting PSD Measurement Error

During the operation of a wind turbine, various environmental factors can lead to measurement errors, especially when measuring main shaft displacement. First, errors in the signal processing unit may arise from factors such as circuit noise and stray light interference, which are particularly significant during high-speed operation or under complex operating conditions. Vibration or electromagnetic interference from the turbine's operation can affect the sensor signals, leading to measurement inaccuracies. Secondly, the nonlinear characteristics of the PSD sensor can also contribute to measurement errors. Due to material inhomogeneity or edge effects, the sensor's response may not be entirely linear, which is especially noticeable during turbine operation, particularly with low displacements or high-frequency variations, potentially leading to cumulative errors. Finally, errors related

to testing conditions and sensor assembly are common sources of error during turbine operation. Factors such as the sensor's installation position, orientation, and stability can be influenced by turbine vibrations, temperature changes, and the installation environment, all of which can cause the sensor's output to become unstable, thereby affecting the accuracy of displacement measurements [26]. Therefore, these environmental factors collectively influence the measurement of main shaft displacement during turbine operation, potentially leading to certain measurement errors.

The output electrodes of a two-dimensional PSD have a specific size and shape, and their dimensions are not perfectly geometrically symmetrical. As a result, this can lead to nonlinear output errors in the PSD measurements. To address this, the PSD photosensitive surface is typically divided into two zones, A and B, as shown in Figure 5. The positional accuracy in zone A is higher than in zone B. Typically, zone B exhibits larger nonlinear errors, which can reach up to 3% in some cases, while the typical nonlinear error in zone A usually ranges from 0.1% to 2%. To obtain more accurate measurements for the main shaft displacement momentum, and to make the measurement data in Area B more accurate, it is necessary to correct the PSD measurement values.

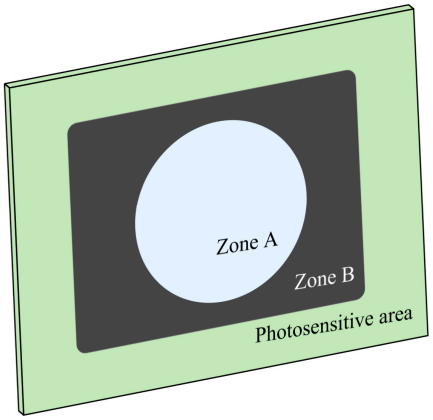

Figure 5. Photodetector surface distribution diagram of PSD.

The nonlinear errors of the PSD are much larger than those caused by circuit errors. These nonlinear errors are primarily due to the non-uniformity of the resistivity across the PSD photosensitive surface. The larger the area of the photosensitive surface with non-uniform resistivity distribution, the higher the nonlinear error in the measurement data. This nonlinear error worsens as the non-uniformity of the PSD surface resistivity increases, and its error characteristics cannot be corrected through hardware compensation. Furthermore, complex environmental factors during turbine operation, such as strong vibrations, temperature fluctuations, and electromagnetic interference, can also affect the performance of the sensor, further exacerbating the non-compensable nature of the nonlinear errors. For example, during high-speed operation of the turbine main shaft, small vibrations or temperature fluctuations may occur, leading to instability in the PSD sensor output and increasing the sources of error.

To improve the output performance and measurement accuracy of the PSD over a wide range, this paper utilizes an SSA-BP neural network to correct the measurement errors of the PSD. This approach helps mitigate the measurement errors caused by the wind turbine's operating environment and sensor nonlinearity to some extent.

4. SSA-BP Neural Network Error Correction Method

With the development of computer network technology and machine learning methods, a large number of scientific approaches with strong nonlinear processing capabilities and real-time learning abilities have emerged. Compared to traditional methods such as table lookup and least squares, BP neural networks offer superior adaptability and nonlinear modeling capabilities. The table lookup method relies on pre-established tables, making it

difficult to handle complex input–output relationships, and updates to the table require manual intervention. Although the least squares method can fit linear models, it performs poorly when dealing with nonlinear data. In contrast, BP neural networks can adaptively learn to address complex nonlinear problems, without relying on predefined tables or linear assumptions [27–29]. This enables more accurate predictions and error correction, making BP neural networks especially suitable for large-scale data or dynamic systems.

4.1. BP Neural Network

The BP neural network is a classic multilayer feedforward neural network model, consisting of an input layer, hidden layer(s), and output layer. Neurons in each layer are only connected to neurons in the adjacent layers, with no connections between neurons in the same layer [30,31]. As shown in Figure 6, the BP neural network structure includes two main stages: forward signal propagation and backward error propagation [32]. The design of a BP neural network involves several key steps: preprocessing sample data, determining the number of hidden layers, selecting the number of neurons, and setting neuron thresholds and weights.

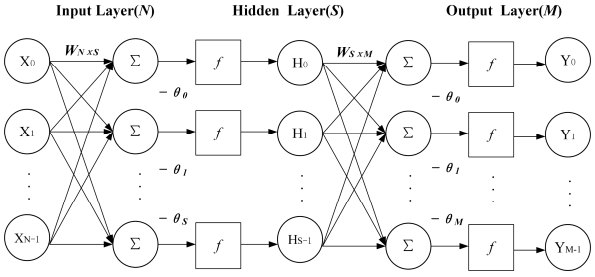

Figure 6. BP neural network structure.

To accelerate the network's convergence, the training sample data for PSD are normalized. This process maps the theoretical calculated position data from PSD and the actual main shaft displacement data to a range between 0 and 1. The network's output data must then be denormalized to restore them to their original scale. The normalization formula is shown in Equation (5).

$$X_k = \frac{X_k - X_{\min}}{X_{\max} - X_{\min}} \tag{5}$$

In the formula, X_k represents the normalized input data for training, while $X_{\max}$ and $X_{\min}$ are the maximum and minimum values of the input training data, respectively.

The number of hidden layers is critical to the accuracy of the model's training. Too few hidden layers may lead to insufficient system accuracy, while too many can cause instability in the error gradient, making the network more prone to getting stuck in local minima. In this system, a single hidden layer structure is adopted.

The number of neurons in the network includes those in the input layer, hidden layer(s), and output layer. The number of neurons in the hidden layer significantly impacts the predictive accuracy of the neural network [33,34]. An empirical formula for estimating the number of hidden layer neurons is provided in Equation (6).

$$L = \sqrt{M + N} + A \tag{6}$$

In the formula, L represents the number of hidden layer neurons, M is the number of input layer neurons, N is the number of output layer neurons, and A is a constant ranging between 0 and 10.

The learning rate is a coefficient that determines the adjustment of weights in a BP neural network, and it directly influences the network's convergence ability and speed. In a typical BP neural network, the thresholds and weights of the neurons are initialized randomly. These random values can affect the recognition accuracy and operating

speed, leading to poor optimization performance after training, slower convergence, and potentially limiting the generalization ability of the model [35,36].

To mitigate the influence of random thresholds and weights during the optimization process, this paper proposes combining the Sparrow Search Algorithm (SSA) [37] with the BP neural network to optimize the network's thresholds and weights. The Sparrow Search Algorithm (SSA), introduced in 2020, is a novel bio-inspired optimization algorithm based on the foraging and anti-predation behaviors of sparrows. It effectively addresses issues such as poor optimization performance and slow convergence speed.

4.2. Sparrow Search Algorithm (SSA)

The SSA is a novel bio-inspired optimization algorithm introduced in 2020, based on the foraging and anti-predation behavior of sparrows. It effectively addresses issues such as insufficient optimization capability and slow convergence speed. Compared to other population-based intelligent algorithms, such as Particle Swarm Optimization (PSO). SSA is a novel population-based optimization algorithm that outperforms traditional algorithms [38].

The foraging behavior of sparrows can be categorized into two main types: predation and anti-predation. Predatory behavior consists of two roles—producers and scroungers. Producers possess more resources and guide the population's search by setting the direction, while scroungers follow the producers, aiding in the collective foraging effort. As they follow, scroungers also increase their own predation rate and, in some cases, monitor the producers to compete for food or forage nearby. The roles of producers and scroungers are dynamic, with scroungers who accumulate more resources transitioning into producers. However, the overall ratio of producers to scroungers remains constant across iterations. Anti-predation behavior is driven by early-warning agents that alert the population to the presence of a predator or any potential danger. When the warning signal exceeds the safe threshold, the producer leads the group to migrate to safer areas. Sparrows at the edge of the group move faster to the safe zones, while those in the middle of the group move randomly to stay with the population. The corresponding mathematical model is as follows:

Producer location updates:

$$X_{i,j}^{t+1} = \begin{cases} X_{i,j}^{t} \cdot \exp\left(-\frac{i}{\alpha \cdot item_{\max}}\right) & if \quad R_2 < ST \\ X_{i,j}^{t} + Q \cdot L & if \quad R_2 \geq ST \end{cases} \tag{7}$$

Let $X_{i,j}^{t+1}$ represent the position of the ith sparrow in the jth dimension at the tth iteration. T is the maximum number of iterations, while Q is a random number drawn from a standard normal distribution. α is a uniformly distributed random number in the range (0, 1], and L is a matrix of size $1 \times$ d, with all elements equal to 1. R_2 is the warning value, and when this value is reached, it indicates that the sparrow population is facing danger and must take protective actions ($R_2 \in [0, 1]$). On the other hand, ST represents the safety threshold, which defines the condition under which the sparrow population can continue its movement without threat (ST $\in$ [0.5, 1]).

$$X_{i,j}^{t+1} = \begin{cases} Q \cdot \exp\left(\frac{X_{\text{worst}} - X_{i,j}^{t}}{i^2}\right) & if \quad i > n/2 \\ X_{p}^{t+1} + \left| X_{i,j}^{t} - X_{p}^{t+1} \right| \cdot A^{*} \cdot L & \text{otherwise} \end{cases} \tag{8}$$

Let X_{p}^{t+1} denote the position of the best producer at the (t + 1)th iteration, and X_{worst}^{t} represent the global worst position at the tth iteration. Q is a random number sampled from a standard normal distribution. A is a $1 \times$ d matrix where each element is randomly assigned either 1 or -1, and $A^{+} = A^{T}(AA^{T})^{-1}$.

Early-warning agent location updates:

$$X_{i,j}^{t+1} = \begin{cases} X_{best}^{t} + \beta \cdot \left| X_{i,j}^{t} - X_{best}^{t} \right| & if \quad f_i > f_g \\ X_{i,j}^{t} + K \cdot \left(\frac{\left| X_{i,j}^{t} - X_{worst}^{t} \right|}{(f_i - f_w) + \varepsilon} \right) & if \quad f_i = f_g \end{cases} \tag{9}$$

Let X_{best} denote the current global optimal position, which is a random value following a normal distribution. K represents the movement direction and step control parameters for the sparrow, with each element of K being $(-1, 1)$ f_i is the adaptation value of the current individual sparrow, f_g is the adaptation value of the current global optimal position, and f_w is the adaptation value of the current global worst position. A small constant is included to prevent division by zero.

4.3. SSA-BP Neural Network

First, the data undergo preprocessing, including denoising, normalization, and standardization, to ensure that the input data to the neural network falls within an appropriate range. The purpose of data preprocessing is to enhance the stability and accuracy of model training. In the optimization of the BP neural network, the "position" of each sparrow individual is considered as the weights and thresholds of the neural network.

Initially, the sparrow population is randomly initialized, with each sparrow's position representing a candidate solution for the neural network (i.e., a set of weights and thresholds). In each iteration, the BP neural network is trained using the current sparrow's weights and thresholds, and the error between the network's output and the target value is calculated, serving as the sparrow's fitness. Based on the update rules of the Sparrow Search Algorithm (SSA), the position of each sparrow is updated, which in turn updates the weights and thresholds of the BP neural network. The updated weights and thresholds are then used to train the BP neural network, with the parameters adjusted through the backpropagation algorithm. Unlike traditional BP training methods, the training process here is driven by the initial solutions and parameter updates provided by the Sparrow Search Algorithm.

This process is repeated, executing the SSA search process until a stopping criterion is met (such as the maximum number of iterations or achieving a certain fitness threshold). After several iterations, the SSA outputs the optimal weights and thresholds, and the corresponding BP neural network becomes the optimal model. The flowchart for SSA-BP neural network-based main shaft displacement prediction is shown in Figure 7.

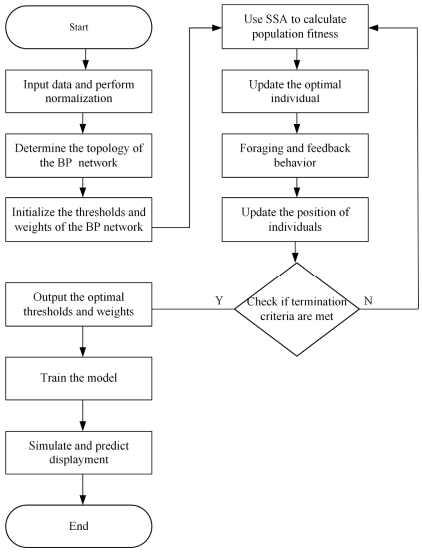

Figure 7. SSA-BP neural network flowchart.

4.4. Algorithm Validation and Analysis

In intelligent optimization algorithms, the fitness function plays a crucial role. Neural networks use the mean squared error (MSE), mean absolute error (MAE), and coefficient of determination (R^2) as model evaluation metrics. Smaller MSE and MAE values indicate a smaller gap between the predicted and actual values, reflecting better model performance. After each iteration, the MSE and MAE values of the neural network are calculated, and the parameters of the neural network are adjusted accordingly to continuously optimize the model's performance. The coefficient of determination (R^2) reflects the model's goodness of fit, with values closer to 1 indicating a higher level of fit.

$$MSE = \frac{1}{n}\sum_{n=1}^{n}\left(y_i - \hat{y_i}\right)^2 \tag{10}$$

$$MAE = \frac{1}{n}\sum_{i=1}^{n}\left|y_i - \hat{y_i}\right| \tag{11}$$

$$R^2 = \frac{\sum_{n=1}^{n}(y_i - \overline{y})^2}{\sum_{n=1}^{n}(\hat{y_i} - \overline{y})^2} \tag{12}$$

In this formula, n represents the number of test samples; y_i denotes the predicted values from the model, $\hat{y_i}$ represents the actual values, and $\overline{y}$ is the mean of the actual values.

To verify the reliability and practicality of the SSA-BP algorithm, a dataset of 90 training samples and 10 testing samples was used for the SSA-BP neural network. The Sparrow Search Algorithm was employed to optimize the initial thresholds and weights of the model. The optimization algorithm uses the mean squared error of both the training and testing sets as the fitness value for SSA, with the fitness function defined as shown in Equation (8).

$$fitness = \text{argmin}(MSE_{Train} + MSE_{Test}) \tag{13}$$

In this formula, MSE_{Train} and MSE_{Test} represent the predicted mean squared error for the training and testing sets, respectively.

To verify the reliability and high performance of the SSA-BP algorithm, the BP neural network, PSO-BP neural network, and SSA-BP neural network were used to train sample sets for both axial and radial main shaft displacement. Due to the different PSD photosensitive surface measurement ranges for axial and radial displacement, separate training was conducted for the respective sample sets. A total of 90 training samples and 10 test samples were used as the neural network dataset. MATLAB 2021was utilized for programming the experiments.

First, training was performed for the axial displacement. As shown in Figure 8a, the conventional BP neural network required approximately 80 iterations to reach a minimum mean squared error (MSE) of 0.0347 mm^2. The PSO-BP neural network required about 62 iterations to achieve an MSE of 0.0156 mm^2, while the SSA-BP neural network achieved a minimum MSE of 0.0123 mm^2 in approximately 51 iterations.

Next, training was conducted for the radial displacement. As shown in Figure 8b, the conventional BP neural network required approximately 78 iterations to reach a minimum MSE of 0.0212 mm^2. The PSO-BP neural network required about 70 iterations to achieve an MSE of 0.0195 mm^2, whereas the SSA-BP neural network achieved a minimum MSE of 0.0086 mm^2 in around 53 iterations.

As shown in Table 1, the accuracy of the SSA-BP model significantly surpasses that of the BP and PSO-BP models. The MSE and MAE of the SSA-BP model are much closer to 0, while the R^2 value is closer to 1 compared to the other two models.

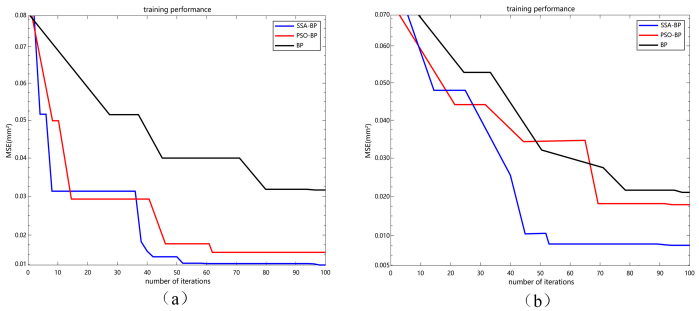

Figure 8. Neural network iteration: (**a**) training results of neural network for axial displacement; (**b**) training results of neural network for radial displacement.

Table 1. Comparison of the evaluation index of each model.

Model	MSE	MAE	R^2
BP	0.0347	0.1863	0.96485
PSO-BP	0.0156	0.1249	0.98345
SSA-BP	0.0123	0.1109	0.99975
BP	0.0212	0.1456	0.96357
PSO-BP	0.0195	0.1396	0.98454
SSA-BP	0.0086	0.0927	0.99987

From the training results for both models, it is evident that the SSA-BP network converges faster, offers higher measurement accuracy, and demonstrates superior correction capability compared to the BP neural network.

After multiple experiments, the optimized weights and thresholds from SSA training were integrated into the model to predict the training samples. For the SSA-BP model of axial displacement, the number of hidden layer nodes was set to 7, with a learning rate of 0.001. The SSA parameters included an initial population size of 30, 51 iterations, a producer ratio of 0.3, and a scrounger ratio of 0.7. Similarly, for the SSA-BP model of radial displacement, the hidden layer nodes were set to 7, the learning rate was 0.001, and the initial population size was 30; 53 iterations were performed, with a producer ratio of 0.3 and a scrounger ratio of 0.7.

5. Experiment Design and Analysis

5.1. Experimental Model Design and Construction

Due to the inability to directly access the top of wind turbine towers, for actual measurements, a laboratory model was used to simulate the main shaft of a wind turbine.

The overall structure of the PSD-based main shaft displacement monitoring platform designed in this paper is shown in Figure 9. The structure consists of a simulated wind turbine main shaft model, a laser, a mirror, a PSD measuring box, and a motion controller (WNSC6000). The PSD, STM32, and AD7606 are all integrated within the measurement box, and the collected displacement data of the main shaft are displayed on a remote computer. The motion controller WNSC6000 controls the electric displacement stages to move in specified directions and displacement values. The experimental model simulating the wind turbine main shaft consists of two angular displacement stages and two electric displacement stages.

A precision displacement stage was employed to simulate the displacement of the wind turbine main shaft. The precision displacement stage provides high-accuracy control, with axial and radial adjustment precision reaching the millimeter level or better, offering a reliable method for replicating the actual displacement of the main shaft. During the simulation process, the displacement parameters of the precision stage were configured based on an analysis of the displacement range of wind turbine main shafts under various operating conditions. The motion patterns of the displacement stage can be flexibly adjusted to mimic the displacement characteristics of the main shaft during different phases, such as

startup, steady operation, variable-speed operation, and shutdown. For instance, during the simulation of the startup phase, the displacement stage can be programmed to gradually accelerate its movement, replicating the transition of a real main shaft from rest to its rated speed, thereby effectively reproducing its motion characteristics.

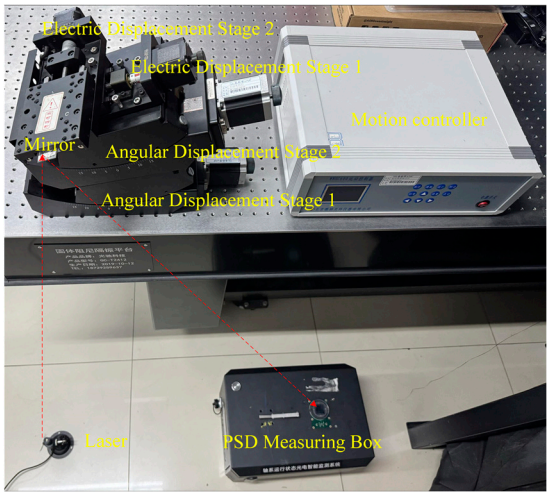

Figure 9. Experimental platform structure.

However, it is important to note that laboratory simulations cannot fully account for the uncertainties encountered by real wind turbines operating in outdoor environments. Extreme weather conditions, such as heavy rain, lightning, and sandstorms, may significantly impact the structural integrity and lubrication state of the main shaft, thereby altering its displacement characteristics. Additionally, due to experimental limitations, certain adverse environmental factors—such as wind and humidity—were not considered in this study, although these factors are critical in real-world wind turbine operations. For example, strong winds can exert additional lateral forces on the main shaft, causing variations in displacement, while high humidity may affect the electrical performance of sensors, reducing measurement accuracy.

While these environmental factors have relatively minor effects on displacement measurements during actual operation—since wind turbines are typically designed with environmental adaptability in mind and are equipped with measures to mitigate extreme conditions—components such as the main shaft and sensors are specially engineered and protected to withstand interference from harsh environments. Nevertheless, these factors should not be overlooked. Future research will aim to replicate more realistic operating conditions in the laboratory. For example, controllable fans can be used to generate artificial wind fields that simulate lateral wind loads on the main shaft, while humidity control systems can be employed to investigate the impact of high-humidity environments on sensor performance. Careful consideration of these factors in future studies and design efforts will ensure the reliability of the system and the accuracy of displacement measurements under varying operational conditions.

Statistical analysis of a large amount of measured data shows that during normal operation, over 98% of the axial displacement data fall within the ± 10 mm range, while over 97% of the radial displacement data lie within the ± 5 mm range. When the axial displacement exceeds ± 10 mm or the radial displacement exceeds ± 5 mm, the alignment between the main shaft and other key components may fail severely, leading to structural instability. Therefore, the electric displacement stages are set to simulate an axial displacement of 20 mm and a radial displacement of 10 mm. Electric Displacement Stage 1 simulates the axial displacement of the main shaft. It is model WN26TA30H, manufactured by Micro Nano Optics Instruments, Beijing, Chinawith a stroke of 30 mm and a resolution of 5 μm. Electric Displacement Stage 2 simulates the radial displacement and is model

WNKS330-10C, also from Beijing Micro-Nano Optics Instruments, with a stroke of 20 mm and a resolution of 5 μm.

According to Equations (2) and (4), the axial and radial displacement momentum of the wind turbine main shaft depend only on the angle θ_1 between the shaft and the ground, and the radial angle θ_2 between the mirror and the main shaft. The two angular displacement stages are responsible for simulating the angles θ_1 (between the shaft and the ground) and θ_2 (between the mirror and the shaft). Both angular displacement stages, model WN06GM30, have a range of $\pm 20^\circ$ and a resolution of 1°.

During the experiment, there may be several potential sources of error, including deviations in the simulation model, inaccuracies in the sensors, and interference from the motion controller. These factors could affect the accuracy and reliability of the experimental results. To enhance the credibility of the research findings, it is essential to identify and briefly discuss these sources of error. For example, deviations in the simulation model may arise from simplifying assumptions or imprecise model parameters, which can be mitigated by more accurate modeling and validation. Inaccuracies in the sensors may result from limitations in sensor precision or changes in environmental conditions, and can be reduced by using higher-precision PSD sensors or by performing calibration. Interference from the motion controller may stem from delays in system response or instability in control signals, which can be minimized by optimizing the control system design and improving hardware stability.

5.2. System Stability Testing

To ensure the system's resistance to interference and long-term stability, conducting stability testing is essential. System stability testing is crucial for the wind turbine main shaft displacement monitoring system, as even small positional errors in the main shaft can significantly affect the overall performance of the system.

The statistical analysis of extensive operational data indicates that a 12 h period is sufficient to capture the various stability characteristics that may arise under sustained operational stress during a complete operational cycle. During this time, critical factors such as the thermal stability of electronic components, the long-term consistency of the data acquisition system, and the reliability of algorithms under prolonged operation can be effectively assessed. The choice of a 30 min measurement interval was made after a thorough evaluation of the system's dynamic response characteristics and data reliability. On the one hand, the displacement of the wind turbine main shaft during normal operation typically changes at a relatively slow rate (excluding sudden fault scenarios). Excessively frequent measurements could introduce unnecessary noise, hindering an accurate assessment of the system's stability. On the other hand, a 30 min interval strikes a balance by allowing for the timely detection of gradual changes over an extended period, such as displacement variations caused by structural thermal expansion due to changing environmental temperatures. At the same time, it ensures efficient data processing and analysis, avoiding an excessive data burden that could strain computational resources.

To evaluate the system's stability, the experimental model was kept stationary, and measurements were taken from the moment the system was started. Data were recorded every 30 min for a continuous 12 h period. As shown in Figure 10, during the initial phase of operation, measurement errors were relatively large due to the instability of the laser intensity and uneven light spots. However, once the laser intensity stabilized, the measurement data remained relatively consistent. The fluctuation range of the light spot was approximately ± 0.024 mm, which meets the system's accuracy requirements.

As shown in Table 2, the precision displacement table was adjusted to different positions, and stability tests were conducted again to measure the position drift at these various points. The position drift remained within ± 0.024 mm across all tests, with no significant increase observed at 1 mm and 17 mm near the edge of the photosensitive surface of the PSD. Compared to the axial displacement range (± 10 mm) and radial displacement range (± 5 mm) of the wind turbine main shaft during normal operation, this fluctuation

range is significantly smaller than the actual displacement range of the main shaft, far exceeding the ±0.05 mm to ±0.08 mm of contact-based methods. This indicates that the system's measurement accuracy under laboratory conditions is far superior to the displacement requirements of the main shaft during normal operation, demonstrating its capability to accurately capture the displacement characteristics of the main shaft in standard operating conditions.

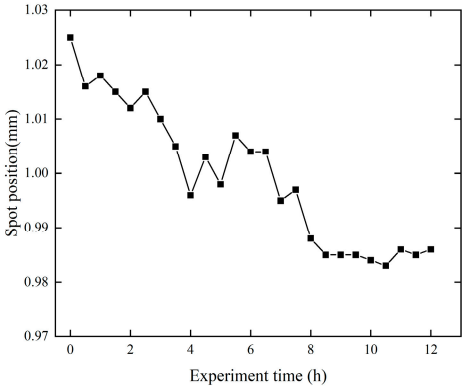

Figure 10. System stability test.

Table 2. Position displacement for different positions.

Spot Position/mm	ΔX/mm
1	±0.024
5	±0.020
9	±0.019
13	±0.021
17	±0.025

5.3. Displacement Measurement Experiment

Absolute error, mean squared error (*MSE*), and maximum nonlinearity error are crucial parameters in monitoring the displacement of wind turbine main shafts. These metrics not only provide a quantitative evaluation of measurement accuracy but also directly impact the reliability of operational state assessments and maintenance decisions. Understanding and minimizing these errors ensure precise displacement measurements, which are essential for maintaining the stability and efficiency of wind turbine systems.

Absolute error is the absolute value of the difference between the measured value and the true value, directly reflecting the degree to which the measurement deviates from reality. In wind turbine main shaft displacement measurements, smaller absolute errors indicate that the measured values are closer to the true displacement of the shaft, which is critical for accurately assessing the operating status of the main shaft. For instance, if the absolute error is too large, it could lead to a misjudgment of whether the shaft is in its normal operating position. In actual operations, if the measured absolute error of the axial displacement of the main shaft reaches a certain level, maintenance personnel may mistakenly believe that the shaft has undergone severe misalignment, prompting unnecessary shutdowns and inspections. This would not only increase maintenance costs but also reduce the operational efficiency of the wind turbine.

The mean squared error (*MSE*) is the average of the squared differences between measured and true values, reflecting both the magnitude and distribution of errors. In wind turbine main shaft displacement measurements, a lower *MSE* indicates higher accuracy and stability, making the results more reliable. Monitoring changes in *MSE* over time can help evaluate the long-term performance of the measurement system. A gradual increase in *MSE* may signal sensor degradation or environmental interference, requiring maintenance or calibration. *MSE* is also useful for comparing different measurement methods; the

approach with the lowest *MSE* ensures optimal performance. In wind farm operations, *MSE* serves as a key indicator for assessing system performance. If *MSE* exceeds a set threshold, corrective actions such as replacing sensors, optimizing the environment, or improving algorithms should be taken to ensure accurate measurements and reliable maintenance decisions.

Maximum nonlinearity error is the largest deviation of measured values from the ideal linear response, indicating the system's degree of nonlinearity. In wind turbine main shaft displacement measurements, this error can result from sensor defects, environmental factors, or system constraints. Significant nonlinearity error introduces systematic bias, especially in large displacement measurements, affecting the accuracy of shaft position or motion assessments and reducing reliability. For instance, during critical startup or shutdown phases, high nonlinearity error may distort the shaft's true motion trajectory. Under extreme conditions, excessive nonlinearity error can amplify deviations, leading to incorrect maintenance decisions. To address this, calibration techniques, nonlinear compensation algorithms, or high-performance sensors should be used. Minimizing this error ensures consistent measurement accuracy across the displacement range, which is vital for real-time monitoring and long-term wind turbine performance evaluation.

To verify the feasibility of the SSA-BP algorithm for error correction, the main shaft model was kept stationary while motorized displacement stages 1 and 2 were controlled to move in 1 mm increments. As indicated by the statistical analysis of measured data discussed earlier, most axial displacement data during normal operation falls within the $\pm$10 mm range, while radial displacement data are typically within the $\pm$5 mm range. To simulate extreme conditions that exceed these normal ranges, an axial displacement of 20 mm and radial displacement of 10 mm were simulated, and the main shaft displacement was measured using three approaches: without a neural network model, with the BP neural network model, and with the SSA-BP neural network model trained earlier.

Figure 11 presents the measurement results of the main shaft displacement without model correction. Figure 11a shows the displacement position comparison data, where the maximum absolute error for axial displacement is 0.72 mm, with a mean squared error (*MSE*) of 0.0787 mm^2. For radial displacement, the maximum absolute error is 0.251 mm, and the *MSE* is 0.0249 mm^2. Figure 11b illustrates the position error distribution across the measurement points. Calculations show that the maximum nonlinearity error rate for the axial displacement measurement system, with a total range of 20 mm, is 3.6%, while the radial displacement measurement system, with a total range of 10 mm, exhibits a maximum nonlinearity error rate of 2.5%. These results indicate that the system error is relatively large without model correction, making it insufficient for high-precision measurement requirements, and highlighting the necessity of error correction.

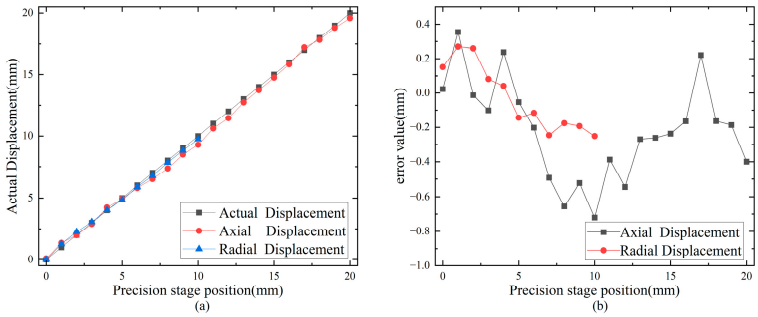

Figure 11. Position measurement results: (**a**) position data comparison; (**b**) position error distribution.

The trained BP and SSA-BP neural network models were implemented on an STM32 microcontroller for measurement. Figure 12 presents the measurement results after correction using BP neural networks and SSA-BP neural networks. As shown in Figure 12a, for axial displacement, the BP neural network correction yields a maximum absolute error of 0.385 mm, a maximum nonlinearity error of 1.925%, and a mean squared error (*MSE*) of

0.0357 mm^2. In contrast, the SSA-BP neural network reduces the maximum absolute error to 0.165 mm, the maximum nonlinearity error to 0.825%, and the *MSE* to 0.0197 mm^2. Compared to the uncorrected results, the SSA-BP correction decreases the maximum absolute error by 0.555 mm and reduces the nonlinearity error by 2.77%. For radial displacement, as shown in Figure 12b, the BP neural network correction results in a maximum absolute error of 0.187 mm, a maximum nonlinearity error of 1.87%, and an *MSE* of 0.0148 mm^2. After correction using the SSA-BP neural network, the maximum absolute error decreases to 0.129 mm, the maximum nonlinearity error to 1.29%, and the *MSE* to 0.0071 mm^2. Compared to the uncorrected results, the SSA-BP correction reduces the maximum absolute error by 0.122 mm and decreases the nonlinearity error by 1.21%.

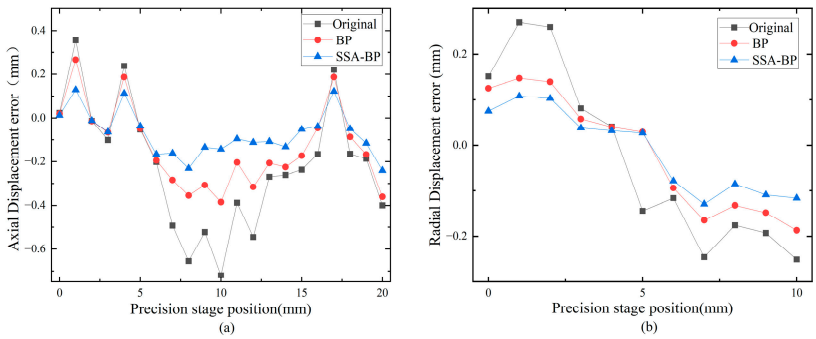

Figure 12. Comparison of position errors before and after correction: (**a**) axial displacement error; (**b**) radial displacement error.

The results clearly demonstrate that the SSA-BP neural network outperforms both the BP neural network and the uncorrected state. The maximum nonlinearity errors for both axial and radial displacements after SSA-BP correction are below 2%, significantly improving the system's linearity and ensuring the measurement results are closer to the ideal linear model. Additionally, the substantial reduction in *MSE* after SSA-BP correction indicates improved anti-interference capabilities and enhanced stability of the system. Furthermore, the SSA-BP algorithm exhibits stronger error correction and prediction performance in complex measurement environments, effectively enhancing the system's accuracy and reliability.

In conclusion, the SSA-BP neural network demonstrates superior performance in correcting the measurement of main shaft displacement. It successfully reduces measurement errors, improves system linearity, stability, and precision, and validates the algorithm's effectiveness and practicality. This provides robust technical support for the high-precision monitoring of main shaft displacement.

5.4. Model Generalization Validation

To verify the generality of the SSA-BP algorithm, another simulated experiment was conducted using the trained BP and SSA-BP models. According to the experimental results, the maximum nonlinearity error for axial displacement measurement after correction was 0.79%, while for radial displacement measurement, it was 1.16%. As shown in Figure 13, a comparison of the correction values between the BP neural network and the SSA-BP network demonstrates that the SSA-BP algorithm provides effective optimization for the nonlinear correction of main shaft displacement, significantly improving the overall measurement accuracy of main shaft displacement.

After successfully validating the versatility of the SSA-BP algorithm in main shaft displacement measurement and its outstanding nonlinear correction capabilities, we are optimistic about its potential applications in a broader range of displacement measurement scenarios for shaft systems. Taking the displacement measurement of the shaft system in large hydropower generators as an example, the shaft system must endure significant hydraulic impacts, mechanical vibrations, and temperature fluctuations during operation.

The displacement characteristics of the shaft system are highly complex and play a critical role in ensuring the safe and stable operation of the generator. Traditional measurement methods often struggle to accurately capture displacement variations under such harsh conditions and are highly susceptible to environmental interference, resulting in significant measurement errors.

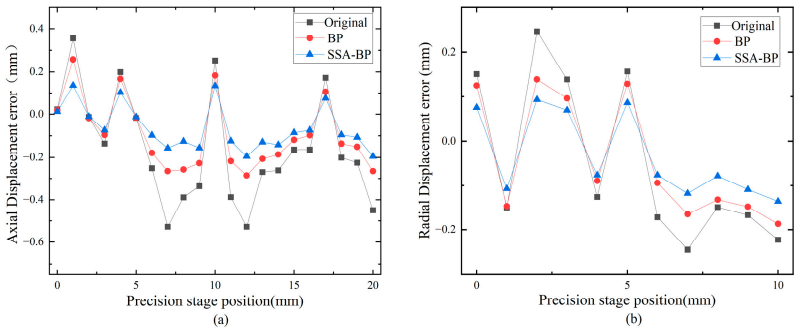

Figure 13. Comparison of errors before and after system calibration. (**a**) axial displacement error; (**b**) radial displacement error.

The SSA-BP algorithm demonstrated in this study, with its strong adaptability and high-precision correction capabilities, offers a novel technical approach to addressing these challenges. We envision applying a similar measurement and correction system to the shaft system monitoring of hydropower generators. By deploying an array of PSD sensors to comprehensively capture displacement information at critical points in the shaft system, and feeding the data into an SSA-BP model specifically optimized through targeted training, the algorithm's exceptional ability to handle nonlinear errors can be leveraged to accurately reconstruct the true displacement state of the shaft system under complex operating conditions. This approach would enable the timely identification of potential issues such as shaft misalignment and bearing wear, providing robust data support for predictive maintenance and the safe, stable operation of the generator.

6. Conclusions

This paper presents a correction method for measuring the displacement error of wind turbine main shafts based on PSD technology. By combining PSD with laser triangulation, the axial and radial displacements of the wind turbine main shaft are measured, and the errors are corrected using an SSA-BP neural network. This approach achieves high stability and precision in displacement measurement.

Experimental results show that the system's stability reaches ± 0.024 mm, far exceeding the ± 0.05 mm to ± 0.08 mm of contact-based methods. After correction, the maximum absolute error for axial displacement is reduced to 0.165 mm, and for radial displacement, it is reduced to 0.129 mm. The maximum linear errors are 0.83% and 1.29%, both below the typical 2% nonlinearity error. Within the normal operating range of the wind turbine main shaft, compared to contact-based measurement methods, this approach offers significant advantages in terms of accuracy, stability, and adaptability to complex environments.

The contribution of this research lies in addressing the challenges of traditional non-contact measurement techniques, particularly their limitations in accuracy and stability under complex environmental conditions. It highlights the advantages of combining the SSA-BP algorithm with PSD and laser triangulation, demonstrating strong generalization capabilities. The proposed method offers a cost-effective and precise solution for main shaft displacement measurement, providing theoretical foundations and technical support for research in the field of wind turbine main shaft displacement monitoring.

Although the experimental results validate the effectiveness of the proposed method, certain limitations remain to be addressed. For instance, in real-world operations, the main shaft of a wind turbine may experience simultaneous axial and radial displacements. This can be addressed by developing an improved model capable of measuring and analyzing

both types of displacement simultaneously. Additionally, we plan to conduct a series of specifically designed experiments to investigate the effects of extreme environmental factors, including wind and humidity. Through these future research efforts, we aim to further enhance the reliability and applicability of the main shaft displacement measurement methods for wind turbines, thereby improving their performance in practical applications.

Author Contributions: Conceptualization, W.Z., L.W. and G.L.; methodology, W.Z. and L.W.; software, W.Z.; validation, W.Z., L.W. and H.Z.; formal analysis, W.Z.; investigation, W.Z. and L.W.; resources, W.Z.; data curation, W.Z.; writing—original draft preparation, W.Z.; writing—review and editing, W.Z., L.W., G.L. and C.P.; visualization, H.Z.; supervision, L.W. and G.L.; project administration, W.Z. and L.W.; funding acquisition, L.W. All authors have read and agreed to the published version of the manuscript.

Funding: This research was funded by the Science and Technology Development Plan of Jilin Province of China under Grant 20220201089GX.

Data Availability Statement: The data are contained within the article.

Conflicts of Interest: The authors declare no conflicts of interest.

References

1. Oh, S.Y.; Joung, C.; Lee, S.; Shim, Y.-B.; Lee, D.; Cho, G.-E.; Jang, J.; Lee, I.Y.; Park, Y.-B. Condition-based maintenance of wind turbine structures: A state-of-the-art review. *Renew. Sustain. Energy Rev.* **2024**, *204*, 114799. [CrossRef]
2. Zhang, Z.Q.; Yin, Z.J.; Han, T.; Tan, A.C.C. Fracture analysis of wind turbine main shaft. *Eng. Fail. Anal.* **2013**, *34*, 129–139. [CrossRef]
3. Yang, W.X.; Tavner, P.J.; Crabtree, C.J.; Feng, Y.; Qiu, Y. Wind turbine condition monitoring: Technical and commercial challenges. *Wind Energy* **2014**, *17*, 673–693. [CrossRef]
4. Rafsanjani, H.M.; Sørensen, J.D. Reliability Analysis of Fatigue Failure of Cast Components for Wind Turbines. *Energies* **2015**, *8*, 2908–2923. [CrossRef]
5. Wang, R.M.; Han, T.; Wang, W.R.; Xue, Y.; Fu, D.Y. Fracture analysis and improvement of the main shaft of wind turbine based on finite element method. *Adv. Mech. Eng.* **2018**, *10*, 1687814018769003. [CrossRef]
6. Asian, S.; Ertek, G.; Haksoz, C.; Pakter, S.; Ulun, S. Wind Turbine Accidents: A Data Mining Study. *IEEE Syst. J.* **2017**, *11*, 1567–1578. [CrossRef]
7. Cheng, J.; He, C.F.; Lyu, Y.; Zheng, Y.; Xie, L.Y. Method for evaluation of surface crack size of wind turbine main shaft by using ultrasonic diffracted waves. *Smart Mater. Struct.* **2020**, *29*, 075009. [CrossRef]
8. Jin, X.; Ju, W.B.; Zhang, Z.L.; Guo, L.X.; Yang, X.G. System safety analysis of large wind turbines. *Renew. Sustain. Energy Rev.* **2016**, *56*, 1293–1307. [CrossRef]
9. Noor-A-Rahim, M.; Khyam, M.O.; Li, X.; Pesch, D. Sensor Fusion and State Estimation of IoT Enabled Wind Energy Conversion System. *Sensors* **2019**, *19*, 1566. [CrossRef]
10. Salameh, J.P.; Cauet, S.; Etien, E.; Sakout, A.; Rambault, L. Gearbox condition monitoring in wind turbines: A review. *Mech. Syst. Signal Process.* **2018**, *111*, 251–264. [CrossRef]
11. Márquez, F.P.G.; Chacón, A.M.P. A review of non-destructive testing on wind turbines blades. *Renew. Energy* **2020**, *161*, 998–1010. [CrossRef]
12. Gryllias, K.; Qi, J.Y.; Mauricio, A.; Liu, C.Y. Condition Monitoring of Wind Turbine Drivetrain Bearings. *J. Eng. Gas Turbines Power-Trans. Asme* **2024**, *146*, 071001. [CrossRef]
13. de Azevedo, H.D.M.; de Arruda, P.H.C.; Araújo, A.M.; Bouchonneau, N.; Rohatgi, J.S.; de Souza, R.M.C. Vibration monitoring, fault detection, and bearings replacement of a real wind turbine. *J. Braz. Soc. Mech. Sci. Eng.* **2017**, *39*, 3837–3848. [CrossRef]
14. Cheng, J.; He, C.; Lyu, Y.; Zheng, Y.; Xie, L.; Wu, L. Ultrasonic inspection of the surface crack for the main shaft of a wind turbine from the end face. *NDT E Int.* **2020**, *114*, 102283. [CrossRef]
15. Jiang, Z.; Huang, X.; Zhu, H.; Jiang, R.; Du, S. A new method for contact characteristic analysis of the tapered roller bearing in wind turbine main shaft. *Eng. Fail. Anal.* **2022**, *141*, 106729. [CrossRef]
16. Selvaraj, Y.; Selvaraj, C. Proactive maintenance of small wind turbines using IoT and machine learning models. *Int. J. Green Energy* **2022**, *19*, 463–475. [CrossRef]
17. Hu, C.; Wang, X.J.; Song, B. High-performance position-sensitive detector based on the lateral photoelectrical effect of two-dimensional materials. *Light-Sci. Appl.* **2020**, *9*, 88. [CrossRef] [PubMed]
18. Zhang, P.C.; Liu, J.; Yang, H.M.; Yu, L. Position Measurement of Laser Center by Using 2-D PSD and Fixed-Axis Rotating Device. *IEEE Access* **2019**, *7*, 140319–140327. [CrossRef]
19. Geng, L.; Cao, G.; Shang, C.; Ding, H. Absolute Photoelectric Encoder Based on Position-Sensitive Detector Sensor. *Electronics* **2024**, *13*, 1446. [CrossRef]

20. Li, J.; Tao, W.; Zhao, H. A Laser Triangulation Displacement Sensor Based on a Cylindrical Annular Reflector. *Photonics* **2023**, *10*, 1139. [CrossRef]
21. Hošek, J.; Linduška, P. Simple Modification of a Commercial Laser Triangulation Sensor for Distance Measurement of Slot and Bore Side Surfaces. *Sensors* **2021**, *21*, 6911. [CrossRef] [PubMed]
22. Lü, Q.N.; Ge, B.Z.; Yao, W.D.; Zhang, Y.M. A method for measuring the thickness of transparent oil film on water surface using laser trigonometry. *Opt. Lasers Eng.* **2011**, *49*, 13–15. [CrossRef]
23. Siddiqui, M.O.; Feja, P.R.; Borowski, P.; Kyling, H.; Nejad, A.R.; Wensk, J. Wind turbine nacelle testing: State-of-the-art and development trends. *Renew. Sustain. Energy Rev.* **2023**, *188*, 113767. [CrossRef]
24. Salic, T.; Charpentier, J.F.; Benbouzid, M.; Le Boulluec, M. Control Strategies for Floating Offshore Wind Turbine: Challenges and Trends. *Electronics* **2019**, *8*, 1185. [CrossRef]
25. Lonescu, L.; Pontius, T. The wind turbine main shaft with one end bearing floating and the other end bearing fixed. *J. Electr. Eng.* **2010**, *3*, 50–53.
26. Cheng, Y.B.; Luo, P.H.; Shen, B.; Wang, Y.H.; Li, Y.R.; Li, S.H. Analysis of Long-Distance Geometric Error Measurement and Uncertainty Based on PSD Laser Collimation Principle. *Photonics* **2024**, *11*, 538. [CrossRef]
27. Han, S.; Xu, J.; Yan, M.; Liu, Z. Using multiple linear regression and BP neural network to predict critical meteorological conditions of expressway bridge pavement icing. *PLoS ONE* **2022**, *17*, e0263539. [CrossRef]
28. Tang, X.P.; Liu, H.J.; Feng, D.X.; Zhang, W.J.; Chang, J.; Li, L.; Yang, L. Prediction of field winter wheat yield using fewer parameters at middle growth stage by linear regression and the BP neural network method. *Eur. J. Agron.* **2022**, *141*, 126621. [CrossRef]
29. Lu, Y.; Li, Z.; Zhao, X.; Lv, S.; Wang, X.; Wang, K.; Ni, H. Recognition of Rice Sheath Blight Based on a Backpropagation Neural Network. *Electronics* **2021**, *10*, 2907. [CrossRef]
30. Parisi, G.I.; Kemker, R.; Part, J.L.; Kanan, C.; Wermter, S. Continual lifelong learning with neural networks: A review. *Neural Netw. Rev.* **2019**, *113*, 54–71. [CrossRef] [PubMed]
31. Zhu, H.L.; Wang, Y.S. Intelligent Prediction of Prestressed Steel Structure Construction Safety Based on BP Neural Network. *Appl. Sci.* **2022**, *12*, 1442. [CrossRef]
32. Li, X.Y.; Yuan, C.H.; Shan, B.N. System Identification of Neural Signal Transmission Based on Backpropagation Neural Network. *Math. Probl. Eng.* **2020**, *2020*, 9652678. [CrossRef]
33. Song, X.D.; Yang, W. Research on the Sound Quality Evaluation Method Based on Artificial Neural Network. *Sci. Program.* **2022**, *2022*, 8686785. [CrossRef]
34. Wang, D.; Lu, H.C.; Yang, M.H. Online Object Tracking With Sparse Prototypes. *IEEE Trans. Image Process.* **2013**, *22*, 314–325. [CrossRef]
35. Oh, S.H.; Lee, Y. Sensitivity analysis of single hidden-layer neural networks with threshold functions. *IEEE Trans. Neural Netw.* **1995**, *6*, 1005–1007. [CrossRef] [PubMed]
36. Piche, S.W. The selection of weight accuracies for Madalines. *IEEE Trans. Neural Netw.* **1995**, *6*, 432–445. [CrossRef]
37. Xue, J.K.; Shen, B. A survey on sparrow search algorithms and their applications. *Int. J. Syst. Sci.* **2024**, *55*, 814–832. [CrossRef]
38. Zhang, J.; Zhu, X.; Li, J. Intelligent Path Planning with an Improved Sparrow Search Algorithm for Workshop UAV Inspection. *Sensors* **2024**, *24*, 1104. [CrossRef] [PubMed]